How the surface state of nickel/gadolinium-doped ceria cathodes influences the electrochemical performance in direct CO 2 electrolysis

Dingkai Chen, Dimitrios K Niakolas, Vasiliki Papaefthimiou, Evangelia Ioannidou, Stylianos G Neophytides, Spyridon Zafeiratos

How the surface state of nickel/gadolinium-doped ceria cathodes influences the electrochemical performance in direct CO_2 electrolysis

Dingkai Chen[a], *Dimitrios K. Niakolas*[b], *Vasiliki Papaefthimiou*[a], *Evangelia Ioannidou*[b], *Stylianos G. Neophytides*[b,**] *and Spyridon Zafeiratos*[a,*]

[a]Institut de Chimie et Procédés pour l'Energie, l'Environnement et la Santé (ICPEES), UMR 7515 du CNRS-UdS 25 Rue Becquerel, 67087 Strasbourg, France

[b]Foundation for Research and Technology, Institute of Chemical Engineering Sciences (FORTH/ICE-HT), Patras, GR-26504, Greece

AUTHOR INFORMATION

Corresponding Author

*spiros.zafeiratos@unistra.fr.

**neoph@iceht.forth.gr

Abstract

The effect of the surface state on the electrochemical performance of nickel gadolinium-doped ceria (NiGDC) cermet electrodes in direct CO_2 electrolysis was studied by *operando* near ambient pressure X-ray photoelectron spectroscopy combined with *on-line* gas phase and electrical measurements. The CO_2 electrolysis was limited at overpotentials below the carbon deposition threshold to avoid irreversible cathode deactivation. The results revealed the dynamic evolution of the NiGDC electrode surface and disclose the side reactions associated to electrode activation in CO_2 electrolysis. Comparison of reduced and oxidized electrodes shows that metallic Ni is a prerequisite for CO_2 electrolysis, at least at low potentials, suggesting that CO_2 electoreduction occurs primarily at the three phase boundaries between gas, metallic nickel and partially reduced ceria. We also provide evidences of *in situ* reduction of NiO upon polarization in CO_2, implying that addition of reductive gases to CO_2 is not indispensable to maintaining the cermet electrode in the reduced state. Inspired by this observation, we use a conventional button cell setup to demonstrate improved *i*-V characteristics of NiGDC electrodes in direct CO_2 electrolysis as compared to CO_2/H_2 fuel conditions and we rationalize this behavior based on NAP-XPS results.

Keywords: Operando spectroscopy, solid oxide cells, cermet electrodes, NiGDC, X-ray photoelectron spectroscopy, CeO_2, mechanism, high temperature electrolysis.

1. Introduction

CO_2 is the most common environmental pollutant and is considered largely responsible for global warming through the "greenhouse effect". In recent years, there is increasing interest to consider CO_2 as resource rather than waste, and transform it catalytically to value-added chemicals and fuels [1,2]. In order to convert CO_2 to higher-value products, it should be first transformed to a more chemically active molecule, for example carbon monoxide. Electrolysis of CO_2 to CO at elevated temperature using solid oxide electrolysis cells (SOEC) appears as a very promising solution for large-scale energy storage [3–8], since it offers higher energy efficiency as compared to low temperature conversion methods. In addition, simultaneous electrolysis (co-electrolysis) of steam and CO_2 is an alternative route to directly produce synthesis gas (i.e. CO and H_2) from non-fossil fuel sources [9,10].

Despite the great efforts devoted to the design and preparation of new electrocatalysts with high activity and stability, composites of ceramic and metal (cermets) that have been previously optimized for solid oxide fuel cells (SOFC), remain the state-of-the-art (SoA) cathode electrodes for SOEC as well [9,11]. The two principal SoA cermet cathode electrodes are nickel composites with yttria stabilized zirconia (NiYSZ) or gadolinium doped ceria (NiGDC). Ni oxidation and carbon formation of Ni-based cermet cathodes during CO_2 electrolysis are related to cells and stacks performance degradation [3,9,12]. To prevent Ni oxidation a reductive gas, such as H_2 or CO, is typically mixed with CO_2 [6,10]. However, recent studies demonstrated a stable operation in *direct* CO_2 electrolysis [13–15]. Please note that the term "direct" [16], or sometimes also called "pure" [13], or "without safe gas" [15,17] CO_2 electrolysis, refers to feed conditions where CO_2 is not mixed with a reductant gas.

Carbon formation on Ni and ceria containing electrodes is attributed mainly to the Boudouard reaction ($2CO \rightarrow CO_2 + C$), while direct electrochemical carbon deposition reactions are also possible [18]. In this respect, C. Graves and coworkers demonstrated that cells with GDC cathodes can operate steadily in CO_2/CO mixtures, while in similar conditions their Ni/YSZ equivalents are rapidly deactivated due to carbon deposition [5].

Although significant effort has been devoted to understand the carbon deposition mechanism during CO_2 electrolysis over Ni-based cathodes [5,12,18–25], the effect of the electrode surface state in the electrocatalytic performance is much less studied. Typically, literature considers that the active electrode area of NiYSZ is the convergence of Ni, YSZ and gaseous phase, the so-called three-phase boundaries (TPBs), while for NiGDC, the mixed ionic electronic conduction of GDC allows the reaction to take place at the two-phase boundary (2PBs) between GDC and the gas phase [3,11]. Cells composed of porous doped-ceria fuel electrodes, i.e. without nickel, show considerable CO_2 electrolysis activity and stability [5], while the primary role of 2PBs on GDC, as compared to TPB, was also proposed as well for H_2O electrolysis [26] and H_2 electroxidation [27] reactions. The aforementioned observations put into question the essential role of nickel in electrochemical reactions over NiGDC, which is somehow surprising considering that SoA NiGDC electrodes are composed of 65 wt.% nickel.

We have previously studied the role of nickel surface state in the electrocatalytic performance of NiGDC electrodes during H_2O electrolysis [26,28], showing that partially oxidized nickel does not lead to deactivation, but on the contrary, can be even beneficial for the cell performance. The aim of the present work is to examine how nickel and ceria oxidation states affect to the CO_2 electrolysis performance and, in particular, to find evidences about the role of nickel in the reaction. To do so, we combine *operando* near ambient-pressure X-ray

photoelectron spectroscopy (NAP-XPS) with *online* gas phase and electrical measurements over cells with porous NiGDC cathodes. It is important to underline that, contrary to the majority of CO_2 electrolysis NAP-XPS studies which concentrate to the carbon deposition mechanism [5,20,23,24,29–32], here we employed operational conditions bellow the carbon deposition threshold, in order to focus on the surface oxidation state and lift complications related to modifications due to irreversible carbon deposition.

2. Materials and Methods

2.1 Fabrication of cells for NAP-XPS experiments

The cell was composed of a 40 μm thick $NiO/Gd_{0.1}Ce_{0.9}O_2$ (65/35 wt.% ratio) cathode (fuel electrode) with mass loading of approx. 25 mg/cm^2, deposited by screen printing method directly on a 300 μm thick 8YSZ electrolyte (Kerafol GmbH). A Pt layer on the reverse side, deposited by magnetron sputtering, was acting as the anode (O_2 electrode). The samples were sintered in air at 1250 °C for 5 h. Due to limitations related to the NAP-XPS sample holder dimensions, fragments of button cells with geometric surface area of about 0.35 cm^2 were used for the NAP-XPS measurements.

2.2 Preparation of NiO/GDC//8YSZ//GDC/LSCoF cells for electro-catalytic measurements

The single SOEC comprised of circular shaped planar 8YSZ electrolyte-supported membranes (Kerafol GmbH) with a diameter of 25 mm and thickness of 150 μm. Commercial NiO/GDC (65 wt.% NiO – 35 wt.% $Ce_{0.9}Gd_{0.1}O_{2-x}$, Marion Technologies) was used for the fuel electrode-paste preparation, by means of the screen printing method. The loading of the examined NiO/GDC electrode was 10 mg/cm^2 with 1.8 cm^2 geometric surface area and a thickness of approximately 40 μm. The anode (O_2) side was a porous $La_{0.6}Sr_{0.4}Co_{0.8}Fe_{0.2}O_{3-\delta}$

(LSCoF) (provided by SOLIDpower). This anode electrode was also applied by means of screen printing and the final loading was 10 mg/cm^2. Furthermore, an adhesion layer (5 mg/cm^2) of GDC was used between the LSCoF electrode and YSZ electrolyte in order to overcome the thermal and chemical mismatch of the two materials. After screen printing of the electrodes, the cells were sintered at 1150 ^{o}C for 2 h with a heating and cooling ramp rate of 2 ^{o}C/min.

2.3 Quasi in situ and ex-situ electrode characterization

The *quasi in situ* laboratory-based XPS measurements were carried out in an ultrahigh-vacuum (UHV) setup coupled with a variable-pressure reactor (VPR) described in details elsewhere [33,34]. The cell was mounted on a sample holder equipped with a boron nitride heater and a K-type thermocouple. Pre-reduced NiGDC electrodes were exposed to pure CO_2 at pressures ranging from 1 mbar to 1000 mbar and at 700 °C for 60 min. Consequently the VPR was evacuated and the sample was transferred under vacuum to the XPS chamber for analysis. During XPS measurements the sample temperature was maintained at 240 °C to avoid electrostatic charging problems. X-ray diffraction patterns were measured *ex situ* after electrode gas treatments in a Bruker D8 advance diffractometer using Cu Kα radiation.

2.4 Operando NAP-XPS measurements

Operando ambient pressure X-ray photoelectron spectroscopy measurements (NAP-XPS) were performed at ISISS beamline at BESSY synchrotron radiation facility at the Helmholtz-Zentrum-Berlin. The cell was fixed with two metal mounting clips on a stainless steel plate which were also used as the current collectors. Heating was performed from the rear using an IR-laser, while the temperature was measured with a K-type thermocouple. The gas flow into the reaction cell was controlled by calibrated mass flow controllers and the gas phase was monitored *online* by a quadrupole mass spectrometer (QMS-Prisma Pfeiffer). Electrical potentials were applied

between the working and the counter electrodes and the current flow was measured using a computer controlled Autolab potensiostat/galvanostat. The working electrode was grounded, and voltage was applied to the counter electrode in order to avoid electrostatic energy shifts. Initial annealing of the sample in 0.2 mbar O_2 was used to eliminate residual carbon from the surface and after this procedure the C 1s signal was within the noise level during all experiments. Consequently the cell was subjected to reducing, humid and oxidizing pretreatment *in situ*. Prior to the CO_2 electrolysis measurements, the cell was stabilized in CO_2 atmosphere for about 30 min, and consequently a constant cathodic potential was applied stepwise between the anode and the cathode (negative electrode) and the cell current was recorded. The cell was maintained for about 20 min in each potential step to record a full set of NAP-XPS spectra (Ni 2p, Ce 3d, C 1s, O 1s and the Fermi edge). The stability of the surface in a given applied potential was verified by repeating Ce 3d and Ni 2p spectra at the beginning and at the end of the applied potential period. In this work, Ce 3d and Ni 2p spectra recorded at the end are shown to assure that the electrode had reached steady-state. Eventual photon beam damage effects were tested by shifting the analysis spot to a new sample position during measurements, but no major differences were detected in the spectra indicating X-ray beam stability and homogeneity of the elecrtodes. The samples did not exhibit any electrostatic charging under open circuit conditions and the binding energies (BEs) are presented as measured without any correction.

For the electrolysis experiments in the NAP-XPS chamber the cell was heated at 700 °C in 0.1 mbar CO_2 and polarized stepwise from open circuit (O.C.) until 1.5 V (*upward curve*) and then decreased back again to O.C. (*downward curve*). Please note that since only cathodic polarization was applied, the negative sign of the voltage is omitted for clarity. The experimental routine was applied identical for cells pre-reduced in H_2 and pre-oxidized in H_2O. The current

density (*i*) reported in the paper, is the average current density in a period of constant applied potential and it was calculated from integration of current *i vs time* curve *(in* C/cm^2*)* divided by the duration that the potential was applied (in s). A similar procedure was used to calculate the average QMS signal of CO and O_2 at each potential.

2.5 NAP-XPS data analysis

Shirley and liner-types background subtraction and peak fitting of the spectra were done with the software package Casa XPS vs. 2.3. The analysis of the Ni 2p and Ce 3d region is complicated by the overlapping of Ce^{4+}, Ce^{3+}, Ni^{2+} and Ni^0 photoemission peaks. In the present work the contribution of each species oxidation state in the overall spectrum was estimated by a linear combination of spectra measured at the same spectrometer over standard reference samples [35,36]. More details about the fitting procedure are given in ESI 1. For the quantitative calculations the photon flux and the photo-ionization cross-sections were taken into account [37]. The stoichiometries of nickel (NiO_x) and ceria (CeO_y) oxides were calculated from the contribution of Ni^0, Ni^{2+} and Ce^{3+}, Ce^{4+} components in the Ni 2p-Ce 3d spectrum by using the formulas given in ESI 1 [35,38].

2.6 Electro-catalytic testing of of NiO/GDC//8YSZ//GDC/LSCoF cells

The electrocatalytic experiments were accomplished at 900 ^oC under two gas mixtures at the fuel electrode side: (i) 74 vol.% He − 24 vol.% H_2O – 1 vol.% H_2 and (ii) 75 vol.% He – 25 vol.% CO_2. The oxygen compartment was exposed to pure O_2 (F_{tot}=150 cm^3/min). Ni and Pt meshes were used as current collectors on the fuel and oxygen electrode side, respectively [39]. Before each electrochemical measurement, the fuel electrode was pre-reduced for 12 h under 100 vol.% H_2 at 900 ^oC. The flow rate was fixed at 150 cm^3/min in order to avoid any mass transfer limitation effects in the reactor. Polarization i-V curves were recorded by using an AUTOLAB

potentiostat/galvanonstat, model: PGSTAT30 with serial number: AUT70964. Specifically, the measurements were carried out by varying the potential between the open circuit potential (O.C.) value and 2.2 V at a scan rate of 5 mV s^{-1}. Specifically, in the case of the H_2 containing mixture, the NiGDC electrode is maintained reduced at constant O.C.=800 mV while in the free-H_2 mixture the electrode was partially oxidized for 5 min by CO_2 approaching O.C. values <-600 mV. Electrochemical impedance spectra (EIS) measurements were recorded in galvanostatic mode at -300 mA (-167 mA cm^{-2}) with an amplitude of 20 mA, in the frequency range between 100 kHz and 20 MHz.

3. Results and discussion

3.1 Interaction of CO_2 with NiGDC without polarization

Initially, we follow the capacity of CO_2 atmosphere to modify the surface oxidation state and composition of NiGDC under the specific conditions of the NAP-XPS experiment. To examine this, the NiGDC was pre-treated in 0.1 mbar H_2, O_2 or H_2O and subsequently the gas atmosphere switched to 0.1 mbar CO_2 at 700 °C. The effect of H_2, O_2 or H_2O pre-treatment on the NiGDC surface state has been discussed in detail previously [35], here we focus on CO_2. Figure 1a shows Ni 2p and Ce 3d NAP-XPS spectra recorded initially in H_2 (hereafter referred as *pre-red.*NiGDC), and subsequently in CO_2, after about 30±5 min at 700° C. In 0.1 mbar CO_2 nickel remains in the metallic state (Ni^0), but ceria undergoes oxidation; from $CeO_{1.61}$ in H_2, to $CeO_{1.71}$ in CO_2 (see bar graphs in Figure 1). Since carbon deposition was not detected in the C 1s region (see ESI 2), ceria oxidation proceeds most probably according to the reaction: $Ce_2O_3 + CO_2 \rightarrow 2CeO_2 + CO$. In the case of O_2 pre-treated NiGDC (Figure 1b), NiO is preserved in CO_2 but ceria is partially reduced from $CeO_{1.89}$ to $CeO_{1.86}$. Finally, a comparable situation was also found for the H_2O pre-treated sample (hereafter referred as *pre-ox.*NiGDC), with NiO remaining stable

while GDC undergoing reduction from $CeO_{1.82}$ in H_2O to $CeO_{1.72}$ in CO_2 (Figure 1b). Overall, nickel oxidation state is not affected under the employed CO_2 treatments, while ceria undergoes either reduction or oxidation depending on its prior oxidation state. Being an oxidant [40,41], CO_2 cannot be accountable for ceria reduction, leaving thermal decomposition of the oxide according to the reaction: $2CeO_2 \rightarrow Ce_2O_3 + ½\ O_2$ as the most likely explanation of the results shown in Figure 1b and 1c.

In general CO_2 is considered capable to oxidize Ni in cermet electrodes [3,40], but contrary to the expected trend under the employed CO_2 conditions, nickel remains metallic. In order to clarify if the resistance of Ni to oxidation by CO_2 is related to the low pressure used in NAP-XPS cell, the dependence of the electrode oxidation state to the CO_2 pressure was examined in a separate experiment. The *pre-red.*NiGDC electrodes were exposed to various CO_2 pressures at isothermal conditions in the VPR reactor [33,34] and consequently transferred under vacuum and characterized by a conventional AlKα monochromatic X-ray source (*quasi in situ* experiments*).* The electrode state measured in the *quasi in situ* experiment is representative of the one in equilibrium with CO_2 as verified in separate experiments discussed in ESI 3.

The evolution of nickel and ceria oxidation states as a function of CO_2 pressure is shown in Figure 1d. From this graph it becomes evident that nickel oxidation begins above 1 mbar CO_2 and increases with the CO_2 pressure. On the contrary, ceria's oxidation state is less affected by CO_2 pressure and remains around $CeO_{1.8.}$ The details behind the CO_2 pressure effect on Ni and ceria oxidation is out of the scope of this work and are discussed elsewhere [42]. However the results in figure 1d provide the link between NAP-XPS results and SOEC tests under atmospheric pressure conditions. In particular, in the button cell direct CO_2 electrolysis tests (1 bar), nickel oxidation by the CO_2 gas is anticipated (section 3.5), while in low pressure *operando*

NAP-XPS experiments (0.1 mbar) the oxidation effect of CO_2 was reproduced by applying NiGDC to an oxidative treatment prior to CO_2 electrolysis (section 3.3).

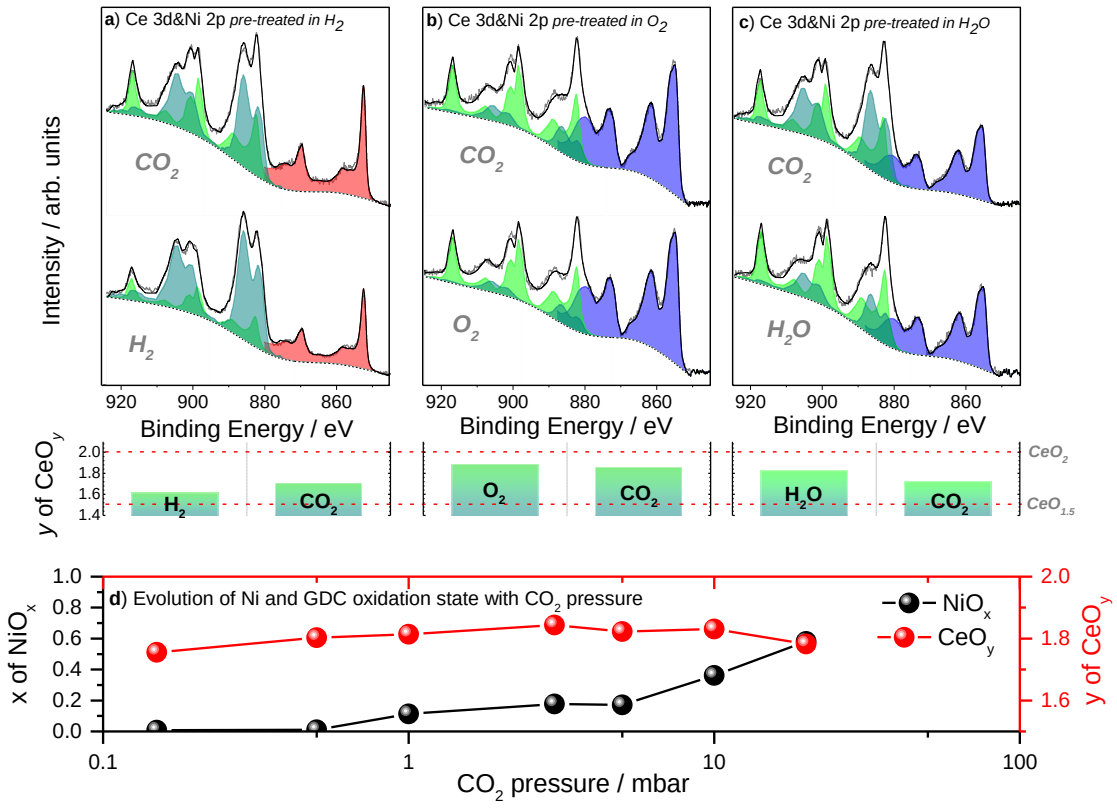

Figure 1. Synchrotron-radiation NAP-XPS measurements for Ce 3d and Ni 2p core-level spectra (hν =1065 eV) recorded in 0.1 mbar of **a)** H_2 and subsequently CO_2 **b)** O_2 and subsequently CO_2 **c)** H_2O and subsequently CO_2 atmospheres. The duration of each treatment was around 30 min while the temperature was kept at 700 °C. The gas and vapor feeds did not include any carrier/inert gas. The deconvolution of the overall peak to metallic Ni^0 (pink), Ni^{2+} (purple), Ce^{3+} (dark green) and Ce^{4+} (light green) is indicated. The mean surface oxidation state of GDC in each condition, calculated from the deconvoluted spectra, is shown in the bar-graph underneath. **d)** The evolution of the surface oxidation state of pre-reduced NiGDC electrodes as a function of CO_2 pressure treatment at 700 °C for 1h obtained by *quasi-in situ* XPS in vacuum using a conventional AlKα monochromatic X-ray source. Spectra were recorded at 235 °C to suppress electrostatic charging.

3.2 Pertinence of NAP-XPS and electrical measurements correlation

The high surface sensitivity is a major advantage of XPS, allowing retrieving specific information from the electrode area where electrochemistry takes place, i.e. the two or three phase boundaries [25]. On the downside, the collected information originates from the outer 2-4 nm of a $40x10^3$ nm thick electrode (see paragraph 2.2 and ESI 4 for a schematic representation), thus roughly from 0.01% of the overall electrode volume. Therefore, prior to any attempt to correlate the chemical state as revealed by NAP-XPS, with the electrochemical performance given by electrical and *on line* gas phase measurements, it is important to address possible differences in the chemical state between the inner (close to the interface with the YSZ electrolyte) and outer (at the surface analysed by NAP-XPS) parts of the electrode.

A key point is to understand whether the electrochemical reaction takes place in a uniform manner within the structure of the porous NiGDC or there is a significant hysteresis between the inner and outer parts of the electrode (Fig. S3). Evidently, only in the former case the NAP-XPS results are representative of the NiGDC electrode in operation. The distribution of the electrocatalytic reaction rate inside the volume of an electrode depends on its mixed ionic-electronic conductivity. In particular, oxygen ions (O^{2-}) must be transported via the ionic GDC phase to the YSZ solid electrolyte, while electrons should be transferred towards the current collector. Due to the fact that the electronic conductivity of the NiGDC is at least by 3 orders of magnitude higher than the ionic [43], electrons are transferred considerably faster than ions. Thus, in order to have even distribution of the electrochemical reaction rate all over the volume of the porous NiGDC, the ionic transfer along GDC should be fast as compared to the electrochemical reaction impedance that takes place at the TPB. This is set out by the "characteristic" current of the electrode (I_{el}) expressed in eq. 1. The I_{el} correlates the ionic

conductivity of the GDC (that dictates the transport rate of O^{2-}) and the tafel slope b (that expresses the losses of the charge transfer process across the electrochemical interface) [44,45].

$$I_{el} = \frac{\sigma_i \, b}{H_{el}} \qquad \text{(eq. 1)}$$

where σ_i, the ionic conductivity of the electrode, H_{el} its thickness and $b = \frac{RT}{\alpha F}$ the Tafel slope. In the present case, for GDC, $\sigma_i = 6\, S/m$, T=973K [46], $R = 8.314 \frac{J}{mol\, K}$, $F = 96485 \ \frac{C}{mol}$ and α is the transfer coefficient, which for a single step two electron charge transfer is set equal to 1 [44].

The characteristic current is the nominal upper current limit, above which, the electrode's performance is dictated by the rate of O^{2-} transfer through the ionic GDC phase. In other words, when the cell operates at currents higher than I_{el} the electrochemical reaction would take place mainly at the NiGDC-electrode/YSZ-electrolyte interface, because O^{2-} from this area can reach faster to the YSZ electrolyte. On the contrary, at currents far below I_{el} the charge transfer rate (i.e. the reaction rate at the NiGDC electrochemical interface) is concomitantly developed all over the electrode's volume.

Using eq. 1 for our NiGDC electrode we found a nominal characteristic current density of 1260 mA/cm^2; which is about 40 times higher than the one reported in the NAP-XPS experiments (see Figs 2 and 3). This fact implies that in the NAP-XPS measurements described below, the current varies linearly along the thickness of the electrode i.e. from the electrolyte to the current collector [44]. Therefore, the electrochemical reaction rate is gradientless within the NiGDC electrode i.e. is uniformly distributed across its whole thickness. In this respect, there is essentially no hysteresis in the reaction taking place at the interface close to the YSZ electrolyte and that occurring on the surface of the electrode, where NAP-XPS is measured.

Accordingly, despite that fact that NAP-XPS characterizes only a tiny fraction of the extreme surface of the electrode, the chemical analysis under the employed conditions is considered representative of the Ni-GDC volume and can be associated with its electrochemical response of the cell.

3.3 CO_2 electrolysis over pre-reduced Ni-GDC electrodes

Figure 2a (*top*) presents the i-V curves of a cell with *pre-red.*NiGDC cathode for the upward (*red*) and downward (*blue*) polarization. The i-V curves of the up and down polarization are almost identical, while a clear change in the slope after 0.5 V characterizes the onset of the electrolysis reaction. The absence of any notable hysteresis in the downward polarization indicates that the cell works reversibly without significant deactivation and rules out carbon deposition. A direct confirmation of this is given by the C 1s spectra shown in ESI 2.

The shift of the Fermi edge upon polarization was measured from valence band spectra recorded with 1065 eV excitation energy. At the maximum applied voltage (1.5 V) the shift or the Fermi edge, in respect to its position just before the onset of the CO_2 to CO electrocatalytic reduction (0.5 V), was around 240±50 mV. This value represents the cathode overpotential [5] and it is free from ohmic loses owed to the ionic resistance of the electrolyte. The onset of carbon deposition is reported between 250 mV and 300 mV over Ni-SDC (samarium doped ceria) electrodes [5], therefore limiting the overpotential to 240±50 mV justifies the absent of deposited carbon in our work.

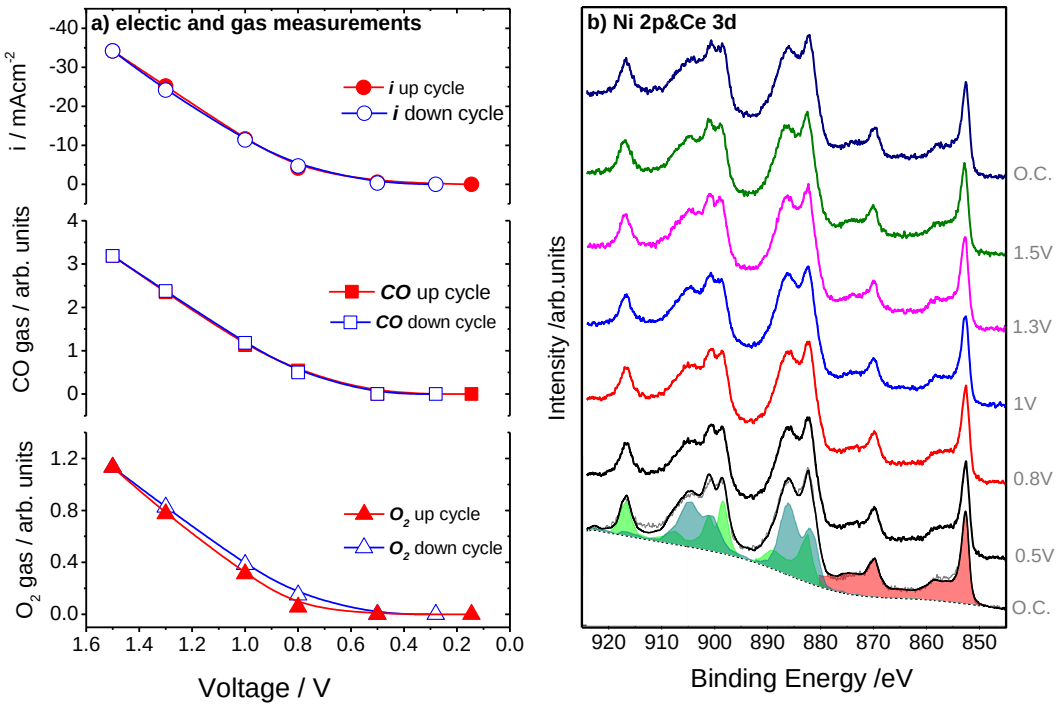

Figure 2. *Pre-reduced NiGDC cathode*. (a) The evolution of the cell current density (top), the CO gas QMS signal (middle) and O_2 gas QMS signal (bottom) as a function of the applied voltage for the up (red) and down (blue) potential curves. (b) Operando NAP-XPS Ce 3d and Ni 2p core-level spectra (hν =1065 eV) recorded under various applied potentials in 0.1 mbar CO_2 at 700 °C. Before electrochemical testing the cell was pre-treated in the spectrometer under 0.1 mbar H_2 at 700 °C for 30 min.

We turn now our attention to the analysis of the gas phase in the NAP-XPS cell. Since this cell is a single chamber reactor (both anode and cathode sides are exposed to the same gas environment), the O_2 produced at the anode (Pt electrode) is detected together with CO produced at the cathode side. Figures 2 *middle* and *bottom* show the CO and O_2 production as a function of the applied bias (the evolution of the QMS signal with time is shown in figure S4). At each applied potential the production of CO is almost identical in the two cycles, while O_2 signal at the up polarization curve is systematically lower than in the down. The Ni 2p and Ce 3d spectra recorded during CO_2 electrolysis are shown in Figure 2b (for the down curve only the O.C.

spectrum is included for clarity). The Ni 2p peak at 852.6 eV is due to Ni^0 and remains stable throughout the experiment [26]. The Ce 3d spectra correspond to a mixed Ce^{4+}/Ce^{3+} state [26] and are slightly influenced by polarization as will be explained in section 3.5.

3.4 CO_2 electrolysis over pre-oxidized Ni-GDC electrodes

Next, we investigate the performance of NiGDC cathodes pre-oxidized *in situ* under mild oxidative conditions (0.1 mbar O_2 and subsequently H_2O at 700 °C). As mentioned in section 3.1 pre-oxidation in the NAP-XPS cell is used to simulate the state of NiGDC electrode after few minutes' exposure in CO_2 under realistic 1 bar operation conditions. According to XRD results (ESI 6), under these conditions nickel in the bulk of the electrode remains partially reduced. The i-V curves shown in Figure 3a (*top*) look very similar to those recorded on the *pre-red.*NiGDC cells. On the contrary, the evolution of the gas products and especially that of CO shown in Figure 3a (*middle and bottom*), seems different in the two polarization curves (the evolution of the QMS signal with time is given in Figure S5). In particular, CO production at the upward polarization starts at 1.3 V, while in the return curve CO is produced down to 0.8 V, similar to the findings of the *pre-red.*NiGDC electrode. The production of O_2 is increasing with the applied voltage, although some differences between the up and down curves can be observed. Notably at 1 V, relatively higher O_2 production is observed at the upward bias. Interestingly, this correlates well with the higher current density measured at 1 V (see i-V curve at the top).

The corresponding Ni $2p_{3/2}$ spectra shown in Figure 3b undergo significant changes upon polarization. Specifically, the initially present Ni 2p spectrum of NiO [28] is preserved up to 1 V, but at higher potentials a characteristic Ni $2p_{3/2}$ component appears at lower energies, indicating partial reduction of NiO to Ni^0. Reduction continues also in the downward polarization and nickel oxidation state is stabilized at about $NiO_{0.4}$. A remarkable observation based on the

comparison between spectroscopic and gas phase results in Figure 3, is that the onset of the electrocatalytic activity (CO production at 1.3 V) and the appearance of reduced nickel peak in XPS coincide. It is worth noticing that although NiO is not completely reduced as in the pre-reduced sample of Fig. 2, the electrocatalytic performance of the pre-oxidized sample is slightly better than that of the pre-reduced one.

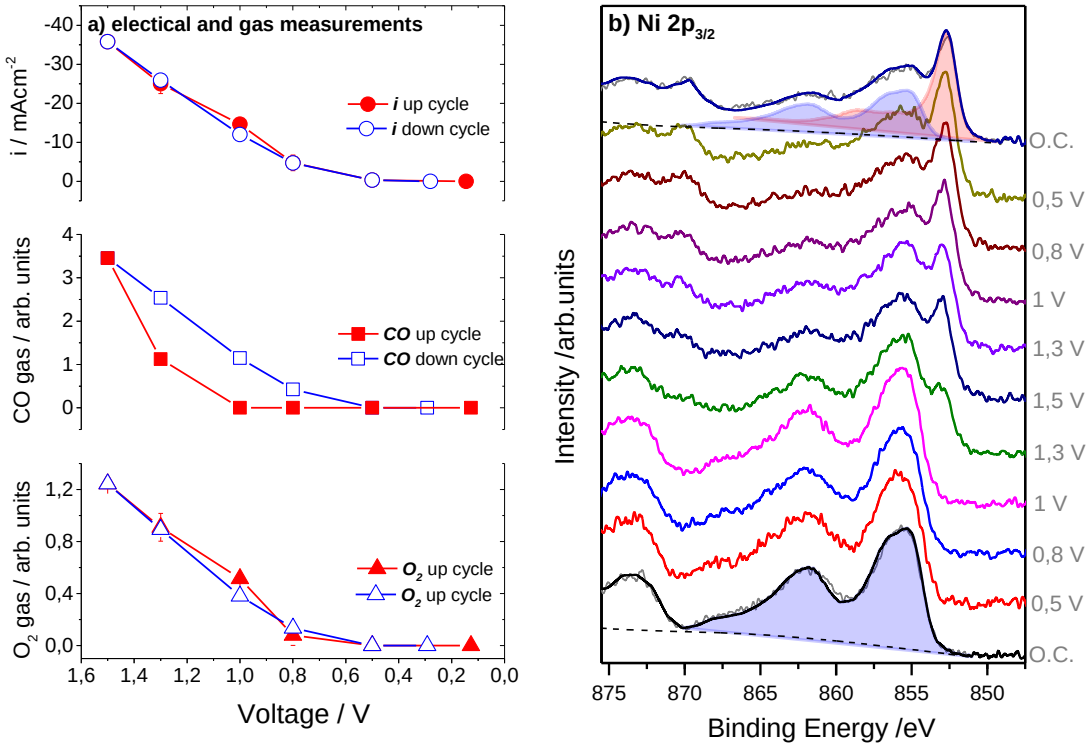

Figure 3. Pre-oxidized NiGDC cathodes (a) The evolution of the cell current density (top), the CO gas QMS signal (middle) and O_2 gas QMS signal (bottom) as a function of the applied voltage for the up (red) and down (blue) potential curves. (b) Operando NAP-XPS Ni $2p_{3/2}$ core-level spectra (hν =1065 eV) recorded under various applied potentials in 0.1 mbar CO_2 at 700 °C. Before electrochemical testing the cell was pre-treated in the spectrometer under 0.1 mbar O_2 at 500 °C and consequently in 0.1 mbar H_2O at 700 °C for a total duration of 1 hour.

Comparison of the Ce 3d and Ni 2p spectra recorded using 2 photon energies, i.e. two information depths [47] (Figure S7 in ESI 7) is used to describe the arrangement of the various

oxidation states. The enhancement of the Ni^0 as compared to Ni^{2+} component at the more surface sensitive mode (1065 eV) suggests that the two oxidation states are arranged in a core-shell like structure with Ni^0 at the shell. Similar analysis of the Ce 3d peak indicates that GDC areas terminate with Ce^{3+} ceria species typically accompanied by a high population of oxygen vacancies [40]. A comparable surface arrangement of NiGDC was found previously for steam electrolysis reaction, indicating that Ni^0/Ce^{3+} is a surface configuration favoured in electrolysis reactions [28,36].

3.5 Correlation of spectroscopic, electrochemical and gas phase results in pre-oxidized and pre-reduced NiGDC.

The O_2 and CO as a function of the cell current for the pre-oxidized and pre-reduced cells are compared in Figure 4a and 4b, respectively. In all cases the production of O_2 (Fig. 4a) with current follows the expected linear relationship, even though in the upward curve of the *pre-red.*NiGDC (*red dash line*) O_2 is systematically lower (see also Figure S4). The evolution of nickel (x of NiO_x) and ceria (y of CeO_y) oxidation states with the current density, estimated from the corresponding photoelectron peaks, is shown in Figures 4c and 4d respectively. As is evident, in *pre-red.*NiGDC ceria undergoes an initial reduction step (red points in Fig. 4c), while the trend is inversed at higher current densities with ceria gradually oxidizing towards an equilibrium oxidation state of $CeO_{1.72}$. Besides, as shown in Figure 4d, the nickel oxidation state of *pre-red.*NiGDC is not influenced throughout the polarization experiment. The stability of metallic nickel, combined to the limited ceria oxidation found by NAP-XPS of *pre-red.*NiGDC electrode, do not allow to attribute the systematically lower O_2 production on this sample (fig. 4a) to consumption via electrode surface oxidation. If such an oxidation takes place, it should

mainly concern the interior parts of the electrode (i.e. bulk) which are not accessible by NAP-XPS, as will be discussed below.

Differences in the gas production between the up and downward polarization were found in the *pre-ox.*NiGDC as well. However, in this case it was not O_2 but CO production which was affected (Figure S5). In particular, as shown in Figure 4b, in the upward polarization CO is either not detected at all or it is lower than the one expected based on the measured current density. The catalytic CO oxidation to CO_2 by gas O_2 (produced on the anode) is not supported by the evolution of O_2 mass signal. More specifically, as shown in figure 4a, O_2 production at the *pre-ox.*NiGDC is proportional to the current density, without any notable differences between the up and down polarization curves. Evidently, in the hypothetical case that O_2 reacts with (two) CO molecules, a decrease in the O_2 production in the upward curve should be observed, which is not the case. Since catalytic CO oxidation is discounted, two different scenarios are put forward to explain the lower CO production observed at the up polarization cycles of *pre-ox.*NiGDC. Carbon monoxide is known to be an efficient reductant for both NiO [48] and ceria [49], so in the first scenario CO is consumed (totally or partially) by reacting with NiO and CeO_2 according to the reactions: $CO+NiO \rightarrow Ni+CO_2$ and $CO+2CeO_2 \rightarrow Ce_2O_3+CO_2$. In the second scenario, current and O_2 on *pre-ox.*NiGDC do not evolve from CO_2 reduction reaction but from another electrochemical reaction that does not involve CO production.

We first examine the compatibility of the first scenario with the NAP-XPS results. Figures 4c and 4d indicate that ceria and nickel oxides are partially reduced during the upward polarization. However, a closer look in the results reveals that reduction starts at current densities > 15 $mA \cdot cm^{-2}$ (corresponding to 1 V in Fig. 3a), but before that nickel and ceria oxidation states remain practically stable. Depth profile (Figure S7) suggested that reduced nickel and ceria

segregate on the surface of the electrode, therefore an eventual reduction of the electrode at low currents should be easily detected in photoemission results. Accordingly, CO consumption due to electrode reduction cannot explain the observations in Figure 4b, at least not for 5 and 15 $mA \cdot cm^{-2}$ (i.e. 0.8 and 1 V).

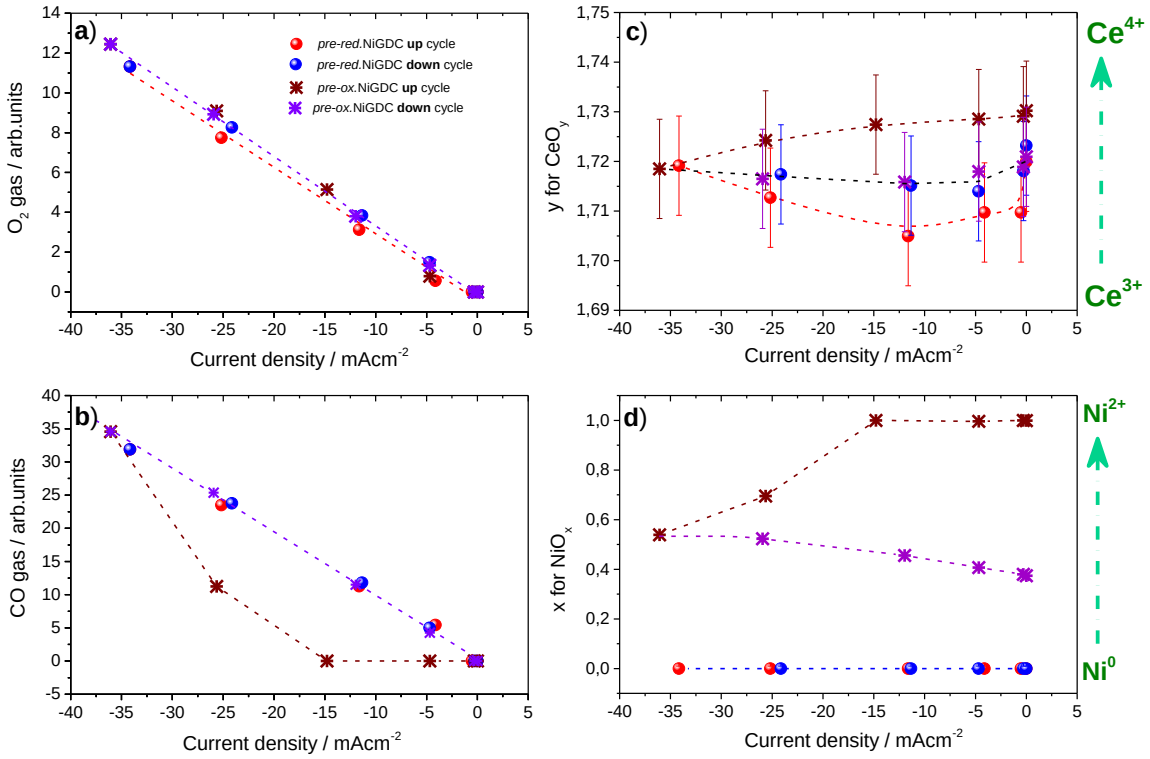

Figure 4. The O_2 gas QMS signal (a), the CO gas QMS signal (b) the mean ceria valence *y*, calculated by the Ce 3d photoelectron peak (c) and the mean nickel valence *x*, calculated by the Ni 2p photoelectron peak (d) as a function of the cell current density. The data were recorded upon cathodic potential in 0.1 mbar CO_2 at 700 °C. The pretreatment and sequence of the recording are provided in figure. The lines serve as a guide to the eye.

Now let us consider the possibility that CO is not consumed, but it is not formed at all at low applied potentials over the *pre-ox.*NiGDC (second scenario). This means that the observed current and O_2 should be produced by an alternative electrochemical reaction. Since the gas feed contains only CO_2, the only possible reactions are the electro-reduction of Ni^{2+} and Ce^{4+} to Ni^0

and Ce^{3+}, respectively. In fact, recent CO_2 electrolysis studies over Ni/YSZ cathodes have shown that electro-reduction of NiO to Ni is possible and thermodynamically more favoured, compared to the CO_2 electrochemical reduction [13].

In order to confirm this argument at the specific conditions of NAP-XPS experiment, we calculated the standard decomposition (R1) and electrolysis (R2) potentials of NiO (E^0_{NiO}) and CO_2 (E^0_{CO2}), using the Nernst's equation (see ESI 8).

$$NiO \rightarrow Ni + \frac{1}{2}O_2 \qquad \text{(R1)}$$

$$CO_2 \rightarrow CO + \frac{1}{2}O_2 \qquad \text{(R2)}$$

According to the calculations, NiO decomposition (R1) will proceed at 370 mV lower applied potential than CO_2 electrolysis (R2). In this respect, the CO_2 electrolysis on oxidized NiGDC electrode surfaces is thermodynamically and kinetically less feasible than the direct electro-reduction of NiO. Thus, it is reasonable to expect that the initiation of the NiO electro-reduction before CO_2 electrolysis and consequently the appearance of measurable reduction current and O_2 signal in Figure 3a at 0.8 V is due to NiO decomposition. This argument is supported by supplementary polarization tests performed in inert gas without CO_2 in the feed (see ESI 9). Note that although both current and O_2 evolution rates increase progressively with time, the metallic Ni component in the XP spectra is not observed before 1.3 V (Fig. 3b). This can be attributed to the fact that oxygen from NiO surface is quickly replaced by the subsurface (bulk) oxygen, which diffuses to the surface with comparable rates to the electrochemical removal of oxygen. In this respect, the electro-reduction process is not detectable by NAP-XPS unless a certain reaction rate is attained (here between 1 and 1.3 V).

At the upward 1.3 V applied voltage, the rate of the evolved O_2 approaches fast to a maximum, which thereafter gradually decreases to increase back again after about 15 min (Figure S5). The

evolution of current follows closely that of O_2, confirming its electrochemical origin. The profile of CO evolution at 1.3 V follows a monotonic increase, which seems not to correlate with O_2 and i evolution. One can rationalize this observation assuming kinetic effects due to the coupling of the R1 (NiO decomposition) and R2 (CO_2 electrolysis) electrochemical processes. In particular, initially R1 dominates producing mainly O_2 and progressively inducing reduction of NiO. The appearance of metallic Ni on the surface promotes R2 therefore CO production rises. When NiO is adequately reduced, the surface is depleted from oxygen, therefore R1 is suppressed and it is R2 that dominates. The rate of the two reactions at each time of the experiment defines the current profile as a function of time. Please note that progressive NiO reduction does not only provide more electroactive sides for CO_2 electrolysis, but is also expected to enhance the electronic conductivity of the electrode. Thereafter, during the application of the higher potential values and by following the downward direction, the current density and the formation rates of CO and O_2 coincide, as expected for the CO_2 electrolysis reaction.

Interestingly, although in the case of the *pre-ox.*NiGDC sample nickel remains partially oxidized, the i-V characteristics of the cell do not deteriorate, but are slightly better than those of the fully reduced *pre-red.*NiGDC (figure S9). The depth profile measurements (figure S7) highlighted that under the aforementioned conditions, a new steady state has been established, having higher degree of oxidation in subsurface layers than on the Ni/NiO surface. This runs counter to the expected trend in which oxide species in vacuum diffuse and accumulate on the surface of the metal due to their lower surface free energy [50,51]. This result can be rationalized by considering that the stronger interaction of CO_2 with Ni^0 species establish a new equilibrium that inhibits the diffusion of oxygen from the inner layers to the outer shell. This can be

attributed to the fact that the surface Ni^0 sites react faster with CO_2 than the diffusion-reaction of O from the interior to the surface.

Eventually we comment on the effect of the pre-treatment (reductive or oxidative) on the oxidation state of ceria observed during polarization. It is clear from Figures 1 and 4c that although ceria's oxidation state is adapted fast to the CO_2 atmosphere, just before polarization, the *pre-ox.*NiGDC electrode remains more oxidized than *pre-red.*NiGDC. However, during the upward polarization, ceria oxidation state is readjusted to an equilibrium sate of $CeO_{1.72}$ and practically remains unchanged in the backward curve independent of the pre-treatment. This is an intriguing finding, which shows that the GDC acts as a source or sink of mobile oxygen ions, by adapting its oxidation state, similar to the well know property of ceria in catalytic reactions [41,52].

3.6 The role of the surface sites on CO_2 electrolysis

Having established the presence of Ni^0 and Ce^{4+}/Ce^{3+} core/shell areas on the NiGDC electrode surface during CO_2 electrolysis, we try now to elucidate the mechanism of the electrochemical reaction on these electrodes. To the best of our knowledge, the CO_2 electrolysis mechanism on NiGDC electrodes has not been described in detail, however studies exist reporting on the reaction mechanism over Ni/YSZ [21,53] and pure ceria [5,54,55] cathodes. Evidently, different reaction sites are involved in the two electrode types, with TPBs and 2PBs credited as the active areas for Ni/YSZ and pure ceria cathodes respectively. Since NiGDC contains both TPBs and 2PBs sites due to the MIEC nature of GDC, one should start with the hypothesis that both type of sites are involved in the reaction, of course depending on their availability. Previous reports have demonstrated that CO_2 reduction reaction on ceria surfaces proceeds through the formation of stable CO_3^{2-} intermediates [5]. The absence of such intermediates shown in ESI 2 suggests that

ceria sites, or in other words 2PBs, are not directly involved in the CO_2 reduction reaction under the employed conditions. Therefore, the reactivity of NiGDC electrode should be attributed to the specific NiGDC interface, or in other worlds to the TPBs sites (Figure 5).

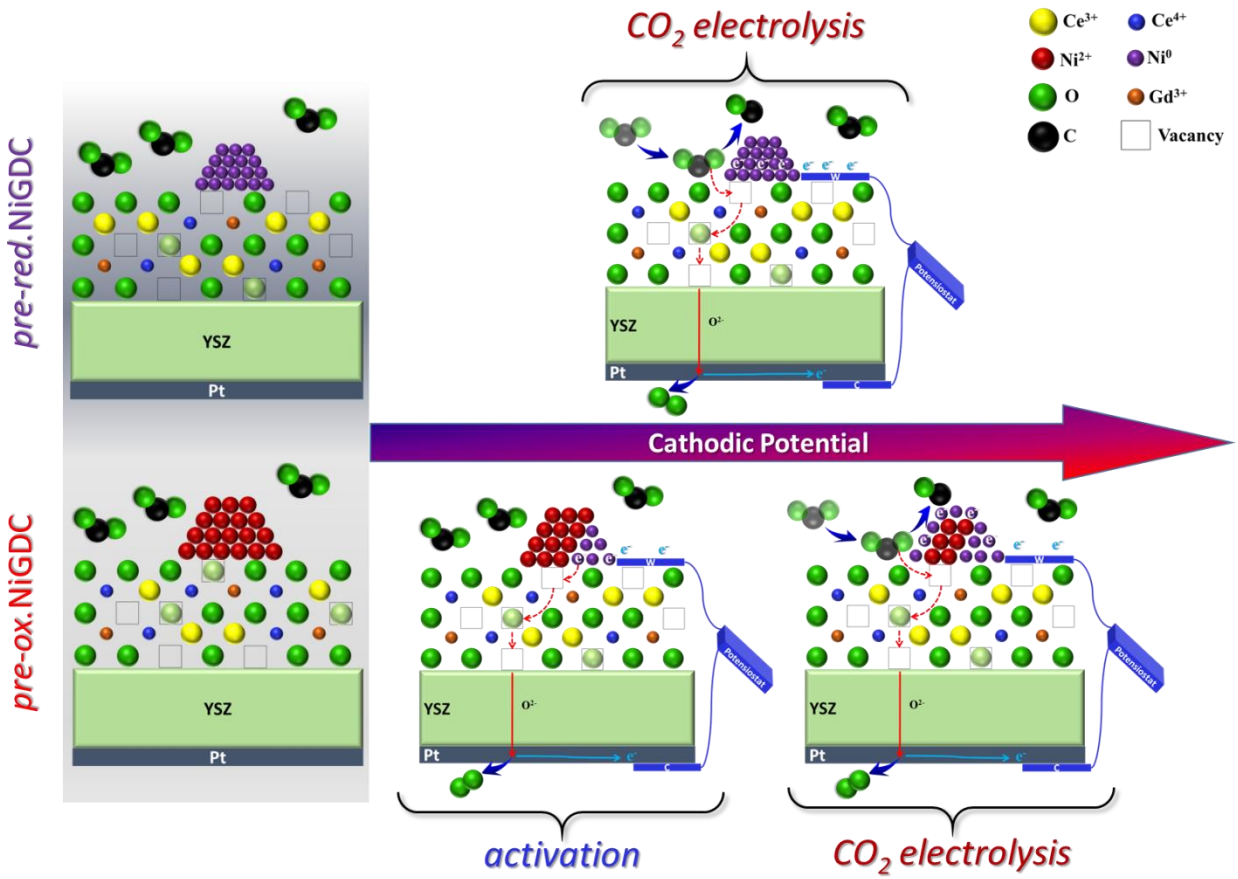

Figure 5. Schematic of the proposed activation and reaction mechanism for reduced and oxidized NiGDC cathodes. In the activation steps electrons flow in the external circuit and gas O_2 is produced but without CO_2 electroreduction.

There are several findings to support this argument. First, on the *pre-ox*.NiGDC, CO is detected parallel to NiO reduction, since electrical conductivity of nickel particles is indispensable for electron transfer at the TPB. On the same electrode, at 0.8 V and 1 V, CO production was observed only at the downward polarization curve after NiO partial reduction. Since in the up and down polarization curves the temperature, gas mixture and applied bias are

identical, one can argue that CO_2 electrolysis does not take place, unless metallic Ni is formed, at least at low potentials. Besides, the similarities of the downward polarization between the two pre-treated electrodes (Figure S9) suggest that partial surface reduction of NiO can be equally beneficial for CO_2 electrocatalysis to the complete Ni^0 reduction. Similar results were previously found also in the case of steam electrolysis on NiGDC electrodes [28].

3.7 Button cell electrochemical tests

The validity of the aforementioned observations regarding the higher activity of partially oxidized nickel cathodes as compared to reduced, was tested using a conventional button cell configuration. Figure 6 shows the i-V curves in the CO_2 electrolysis mode of button cells with pre-reduced NiGDC cathodes recorded with and without H_2 in the feed gas. Both measurements were performed at T = 900 ^oC and ambient pressure, with a faradaic efficiency of ~100% towards the production of CO [13]. The O.C. in the CO_2/H_2 [(●) in Figure 6] is recorded constant at -800 mV, which is normal for an electrode with excess CO_2 in respect to H_2 partial pressure. In case of pure CO_2 [(▲) in Figure 6], the electrode was kept for 5 min at open circuit in order to oxidize nickel surface as suggested by the photoemission results of Figure 1d. The value of the O.C., which dropped below 600 mV, confirms NiO formation (see initial point of (▲) curve). On the contrary to the H_2 containing mixture, the O.C. was not stabilized but kept decreasing below 600 mV after the 5 min passing period (not shown). Surprisingly, the performance of the cell as this is demonstrated by comparison of the i-V curves, is superior in the case of direct CO_2 electrolysis as compared to the CO_2 mixed with H_2. This is in accordance with the findings of NAP-XPS analysis, regarding the enhanced performance of the partially oxidized electrode in respect to fully reduced Ni^0 atoms.

The inset of Figure 6 shows the electrochemical impedance measurements for CO_2 electrolysis with and without H_2 in the feed. The impedance spectra were recorded in galvanostatic mode at similar current density (ca. 167 mA/cm^2), in order to make sure that any observed differences, are due to the variation in the feed conditions of the fuel electrode. Comparison of the two EIS shows a significant decrease of the ohmic resistance of the cell (R_{Ohm}), defined by the high frequency intersect of x-axis, in case of direct CO_2 electrolysis **(▲)** (i.e. partially oxidized electrode). In particular the R_{Ohm} from 4.7 Ωcm^2 in CO_2/H_2 drops to 1.5 Ωcm^2 in CO_2. The polarization resistance (R_p), calculated by the difference between the high and low frequency intercepts of the real axis, does not change significantly in the two reaction conditions (2.4 Ωcm^2 for CO_2 and 2.3 Ωcm^2 for CO_2/H_2). This means that the electrocatalytic activity at the electrochemical interface does not vary to the extent that could justify the significant increase in the performance observed under CO_2 reduction conditions. Thus, the improvement in the performance shown in the i-V curves appears to be related with the significant decrease in the ohmic resistance shown in EIS spectra. Any other effect related to the enhancement of the reaction rate, for example improved diffusivity of the charged species on the Ni particles' surface, is expected to induce noticeable changes in the polarization resistance as well.

The increase of the electronic resistance of a partially oxidized Ni-NiO electrode (in CO_2) as compared to the fully reduced one [**(●)** in CO_2+H_2], runs counter to the inferior electronic conductivity of NiO in respect to Ni. This seemingly contradictory result is, in fact, consistent with our previous studies under H_2O electrolysis showing that partially oxidized Ni-GDC electrodes can better maintain the electron and ion percolation pathways between nickel and ceria particles [28]. In particular, the Ni^0-shell/NiO core morphology of nickel particles during CO_2 electrolysis revealed by NAP-XPS, seems as an optimum structural configuration, since

surface Ni^0 helps to maintain the high electronic conductivity, whereas the NiO core preserves the volume of nickel particles thus sustaining the microstructure of the electrode and the contact between the particles. This is related to the volume expansion of oxidized nickel as compared to metallic Ni^0 [56,57], which helps to sustain the contact areas between the cermet particles, therefore significantly increasing the electrons pathways and compensating the decrease in electron conductivity due to NiO in the inner layers.

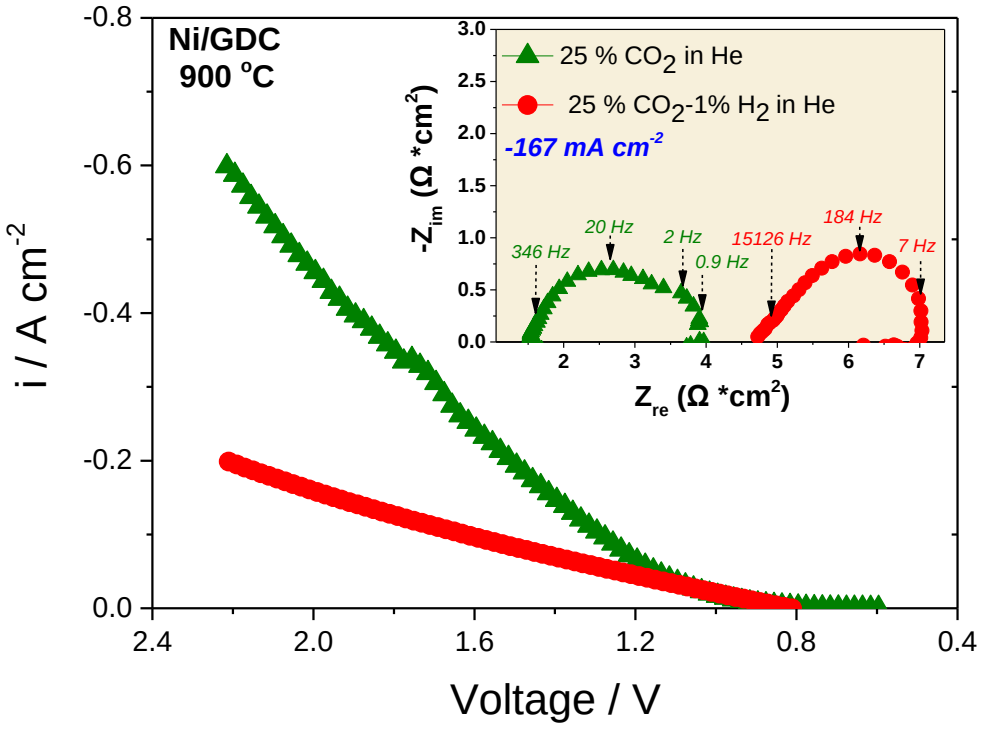

Figure 6. Current-Voltage (i-V) curves recorded in a button cell configuration under ambient pressure and temperature T=900°C for H_2 containing and H_2 free CO_2 mixtures. In the case of the H_2 containing mixture the NiGDC is maintained reduced at constant O.C.= -800mV while in the free H_2 mixture the electrode was partially oxidized for 5min by CO_2 approaching O.C. values <-600mV. *Inset*: EIS measurements (Nyquist plots) of the Ni-GDC||YSZ||$GDC_{barrier}$|LSCoF cell, at 900 °C, under the applied mixtures: (●) 25 vol.% CO_2 – 1 vol.% H_2 – 74 vol.% He and (▲) 25 vol.% CO_2 – 75vol.% He. The spectra were recorded in galvanostatic mode at -167 mA cm^{-2}. F_{total} = 150 cm^3/min.

Long term tests (not presented here), showed that in direct CO_2 electrolysis conditions the performance decreases progressively within a time period of four hours. Although, there are reports of NiYSZ cells with stable operation in direct CO_2 electrolysis for several hours [13], in most studies fast deactivation is observed in electrolysis conditions with little, or not at all, reducing gas in the feed. In particular, despite their promising initial performance for H_2O, CO_2 or H_2O/CO_2 co-electrolysis, Ni-based cermet cathodes either in the form of single cell measurements, or in stacks, usually exhibit poor stability [58–62]. In our case, post mortem cell examination did not give evidences of severe carbon deposition, therefore two deactivation mechanisms can be put forward to explain the above mentioned decrease in the electrochemical performance with time. The most commonly anticipated deactivation cause is related to nickel oxidation in the course of the reaction. Specifically, the high CO_2 content in the reaction mixture may block Ni surface sites, through the formation of strongly adsorbed oxygen species. The latter progressively diffuse from the surface towards the bulk of the electrode forming NiO, decreasing the electronic conductivity. Furthermore, this gradual re-oxidation has been reported to affect the nickel coarsening/agglomeration and finally the volumetric re-structuring of the electrode [63]. Finally the combination of the surface and bulk oxidation deteriorates the performance.

The second deactivation mechanism has its origin on the progressive electro-reduction of NiO particles in the cermet. As explained above the significant volume contraction of nickel particles upon reduction (up to ca. 70%) ([56,57]) will change the NiGDC microstructure and decrease the available electron conduction paths. Macroscopically this is translated to an increase of the electronic (ohmic) resistance of the electrode (the R_{ohm} measured in EIS). In the long term, NiO electro-reduction to Ni^0 progress gradually and the contraction of nickel particles volume is

unavoidable. As a consequence the cell deactivates with time and in its performance converges with this in CO_2/H_2 conditions. The analysis of EIS and NAP-XPS spectra presented above privilege more the electro-reduction deactivation mechanism, however in the absence of direct evidences both mechanisms are credible.

4. Conclusions

Summarizing, *operando* NAP-XPS was applied to examine NiGDC cermet cathodes during CO_2 electrolysis at potentials below the threshold of carbon deposition. It was shown that the functional NiGDC surface consists of metallic nickel and partially reduced ceria. Activation of the CO_2 electrolysis reaction is correlated to electro-reduction of NiO to Ni, which is feasible at relatively low CO_2 electrolysis potentials. Partially reduced nickel particles are organized in a core-shell structure, with metallic nickel in the shell and NiO underneath. Interestingly, formation of a nanometer-thick surface Ni layer is adequate to activate and maintain CO_2 electrolysis, while reduction in deeper NiO layers does not further boost the performance. Improved i-V polarization curves in direct CO_2 electrolysis as compared to CO_2/H_2 fuel conditions were also demonstrated in typical button cell operation conditions. This confirms that direct CO_2 electrolysis over NiGDC cathodes can be attained under selected operation conditions (pressure, applied potential, pretreatment) where the optimal electrode surface state described above is maintained. Our findings provide useful insights for the design of efficient electrochemical devices, particularly for direct CO_2 conversion without reductive gas in the feed.

Acknowledgements

DC would like to thank the China Scholarship Council (CSC) for supporting his studies at ICPEES. Y.T. Law help during BESSY synchrotron measurements is greatly appreciated. The authors would like to thank the *electronic structure* group and especially Dr. Knop-Gericke, Dr

M. Haevecker and Dr D. Teschner, of the Fritz-Haber Institute der MPG and Helmholtz Zentrum, Berlin Germany for providing access at ISISS beamline. The authors would also like to thank Mr. Panagiotis I. Giotakos, MSc. researcher at FORTH/ICE-HT for the constructive comments. Finally, we acknowledge HZB for the allocation of synchrotron radiation beamtime and BESSY Synchrotron staff for the collaboration during the experiments.

References

[1] G. Centi, E.A. Quadrelli, S. Perathoner, Catalysis for CO2 conversion: A key technology for rapid introduction of renewable energy in the value chain of chemical industries, Energy Environ. Sci. 6 (2013) 1711–1731. doi:10.1039/c3ee00056g.

[2] Y.Y. Birdja, E. Pérez-Gallent, M.C. Figueiredo, A.J. Göttle, F. Calle-Vallejo, M.T.M. Koper, Advances and challenges in understanding the electrocatalytic conversion of carbon dioxide to fuels, Nat. Energy. 4 (2019) 732–745. doi:10.1038/s41560-019-0450-y.

[3] Y. Song, X. Zhang, K. Xie, G. Wang, X. Bao, High-Temperature CO2 Electrolysis in Solid Oxide Electrolysis Cells: Developments, Challenges, and Prospects, Adv. Mater. (2019) 1902033. doi:10.1002/adma.201902033.

[4] C. Graves, S.D. Ebbesen, M. Mogensen, K.S. Lackner, Sustainable hydrocarbon fuels by recycling CO2 and H 2O with renewable or nuclear energy, Renew. Sustain. Energy Rev. 15 (2011) 1–23. doi:10.1016/j.rser.2010.07.014.

[5] T.L. Skafte, Z. Guan, M.L. Machala, C.B. Gopal, M. Monti, L. Martinez, E. Stamate, S. Sanna, J.A. Garrido Torres, E.J. Crumlin, M. García-Melchor, M. Bajdich, W.C. Chueh, C. Graves, Selective high-temperature CO2 electrolysis enabled by oxidized carbon intermediates, Nat. Energy. 4 (2019) 846–855. doi:10.1038/s41560-019-0457-4.

[6] S.D. Ebbesen, M. Mogensen, Electrolysis of carbon dioxide in Solid Oxide Electrolysis Cells, J. Power Sources. 193 (2009) 349–358. doi:10.1016/j.jpowsour.2009.02.093.

[7] R. Küngas, Review—Electrochemical CO2 Reduction for CO Production: Comparison of Low- and High-Temperature Electrolysis Technologies, J. Electrochem. Soc. 167 (2020) 044508. doi:10.1149/1945-7111/ab7099.

[8] A. Hauch, R. Küngas, P. Blennow, A.B. Hansen, J.B. Hansen, B. V Mathiesen, M.B. Mogensen, Recent advances in solid oxide cell technology for electrolysis, Science (80-.). 370 (2020) eaba6118. doi:10.1126/science.aba6118.

[9] M. Rao, X. Sun, A. Hagen, Durability of solid oxide electrolysis stack under dynamic load cycling for syngas production, J. Power Sources. 451 (2020) 227781. doi:10.1016/j.jpowsour.2020.227781.

[10] S.D. Ebbesen, R. Knibbe, M. Mogensen, Co-Electrolysis of Steam and Carbon Dioxide in Solid Oxide Cells, J. Electrochem. Soc. 159 (2012) F482--F489. doi:10.1149/2.076208jes.

[11] Y. Jiang, F. Chen, C. Xia, A review on cathode processes and materials for electro-reduction of carbon dioxide in solid oxide electrolysis cells, J. Power Sources. 493 (2021) 229713. doi:https://doi.org/10.1016/j.jpowsour.2021.229713.

[12] W. Yue, Y. Li, Y. Zheng, T. Wu, C. Zhao, J. Zhao, G. Geng, W. Zhang, J. Chen, J. Zhu, B. Yu, Enhancing coking resistance of Ni/YSZ electrodes: In situ characterization,

mechanism research, and surface engineering, Nano Energy. 62 (2019) 64–78. doi:10.1016/j.nanoen.2019.05.006.
[13] Y. Song, Z. Zhou, X. Zhang, Y. Zhou, H. Gong, H. Lv, Q. Liu, G. Wang, X. Bao, Pure CO2 electrolysis over an Ni/YSZ cathode in a solid oxide electrolysis cell, J. Mater. Chem. A. 6 (2018) 13661–13667. doi:10.1039/c8ta02858c.
[14] S. Wang, H. Jiang, Y. Gu, B. Yin, S. Chen, M. Shen, Y. Zheng, L. Ge, H. Chen, L. Guo, Mo-doped La0.6Sr0.4FeO3-δ as an efficient fuel electrode for direct electrolysis of CO2 in solid oxide electrolysis cells, Electrochim. Acta. 337 (2020) 135794. doi:10.1016/j.electacta.2020.135794.
[15] Y. Li, P. Li, B. Hu, C. Xia, A nanostructured ceramic fuel electrode for efficient CO2/H2O electrolysis without safe gas, J. Mater. Chem. A. 4 (2016) 9236–9243. doi:10.1039/C6TA02830F.
[16] Y. Li, B. Hu, C. Xia, W.Q. Xu, J.P. Lemmon, F. Chen, A novel fuel electrode enabling direct CO2 electrolysis with excellent and stable cell performance, J. Mater. Chem. A. 5 (2017) 20833–20842. doi:10.1039/c7ta05750d.
[17] D. Dong, S. Xu, X. Shao, L. Hucker, J. Marin, T. Pham, K. Xie, Z. Ye, P. Yang, L. Yu, G. Parkinson, C.Z. Li, Hierarchically ordered porous Ni-based cathode-supported solid oxide electrolysis cells for stable CO2 electrolysis without safe gas, J. Mater. Chem. A. 5 (2017) 24098–24102. doi:10.1039/c7ta06839e.
[18] T.L. Skafte, P. Blennow, J. Hjelm, C. Graves, Carbon deposition and sulfur poisoning during CO2 electrolysis in nickel-based solid oxide cell electrodes, J. Power Sources. 373 (2018) 54–60. doi:10.1016/j.jpowsour.2017.10.097.
[19] Y. Luo, W. Li, Y. Shi, N. Cai, Mechanism for reversible CO/CO2 electrochemical conversion on a patterned nickel electrode, J. Power Sources. 366 (2017) 93–104. doi:10.1016/j.jpowsour.2017.09.019.
[20] Y. Yu, B. Mao, A. Geller, R. Chang, K. Gaskell, Z. Liu, B.W. Eichhorn, CO2 activation and carbonate intermediates: An operando AP-XPS study of CO2 electrolysis reactions on solid oxide electrochemical cells, Phys. Chem. Chem. Phys. 16 (2014) 11633–11639. doi:10.1039/c4cp01054j.
[21] Y. Luo, Y. Shi, W. Li, N. Cai, Elementary reaction modeling of reversible CO/CO2 electrochemical conversion on patterned nickel electrodes, J. Power Sources. 379 (2018) 298–308. doi:10.1016/j.jpowsour.2018.01.016.
[22] W. Wang, L. Gan, J.P. Lemmon, F. Chen, J.T.S. Irvine, K. Xie, Enhanced carbon dioxide electrolysis at redox manipulated interfaces, Nat. Commun. 10 (2019). doi:10.1038/s41467-019-09568-1.
[23] Z.A. Feng, M.L. Machala, W.C. Chueh, Surface electrochemistry of CO2 reduction and CO oxidation on Sm-doped CeO2-x: Coupling between Ce3+ and carbonate adsorbates, Phys. Chem. Chem. Phys. 17 (2015) 12273–12281. doi:10.1039/c5cp00114e.
[24] J. Wang, S.R. Bishop, L. Sun, Q. Lu, G. Vardar, R. Bliem, N. Tsvetkov, E.J. Crumlin, J.-J. Gallet, F. Bournel, I. Waluyo, B. Yildiz, Threshold catalytic onset of carbon formation on CeO_2 during CO_2 electrolysis: mechanism and inhibition, J. Mater. Chem. A. 7 (2019) 15233–15243. doi:10.1039/C9TA03265G.
[25] Y. Han, H. Zhang, Y. Yu, Z. Liu, In Situ Characterization of Catalysis and Electrocatalysis Using APXPS, ACS Catal. 11 (2021) 1464–1484. doi:10.1021/acscatal.0c04251.
[26] B. Mewafy, F. Paloukis, K.M. Papazisi, S.P. Balomenou, W. Luo, D. Teschner, O.

Joubert, A. Le Gal La Salle, D.K. Niakolas, S. Zafeiratos, Influence of Surface State on the Electrochemical Performance of Nickel-Based Cermet Electrodes during Steam Electrolysis, ACS Appl. Energy Mater. 2 (2019) 7045–7055. doi:10.1021/acsaem.9b00779.

[27] W.C. Chueh, Y. Hao, W. Jung, S.M. Haile, High electrochemical activity of the oxide phase in model ceria-Pt and ceria-Ni composite anodes, Nat. Mater. 11 (2012) 155–161. doi:10.1038/nmat3184.

[28] V. Papaefthimiou, D.K.D.K. Niakolas, F. Paloukis, D. Teschner, A. Knop-Gericke, M. Haevecker, S. Zafeiratos, Operando observation of nickel/ceria electrode surfaces during intermediate temperature steam electrolysis, J. Catal. 352 (2017) 305–313. doi:10.1016/j.jcat.2017.06.005.

[29] B. Bozzini, M. Amati, C. Mele, A. Knop-Gericke, E. Vesselli, An in situ near-ambient pressure X-ray photoelectron spectroscopy study of CO2 reduction at Cu in a SOE cell, J. Electroanal. Chem. 799 (2017) 17–25. doi:10.1016/j.jelechem.2017.05.011.

[30] B. Bozzini, M. Amati, P. Bocchetta, S. Dal Zilio, A. Knop-Gericke, E. Vesselli, M. Kiskinova, An in situ near-ambient pressure X-ray Photoelectron Spectroscopy study of Mn polarised anodically in a cell with solid oxide electrolyte, Electrochim. Acta. 174 (2015) 532–541. doi:10.1016/j.electacta.2015.05.173.

[31] A.K. Opitz, A. Nenning, C. Rameshan, M. Kubicek, T. Götsch, R. Blume, M. Hävecker, A. Knop-Gericke, G. Rupprechter, B. Klötzer, J. Fleig, Surface Chemistry of Perovskite-Type Electrodes During High Temperature CO_2 Electrolysis Investigated by *Operando* Photoelectron Spectroscopy, ACS Appl. Mater. Interfaces. 9 (2017) 35847–35860. doi:10.1021/acsami.7b10673.

[32] S. Hu, L. Zhang, Z. Cao, W. Yu, P. Zhang, X. Zhu, W. Yang, Cathode activation process and CO2 electroreduction mechanism on LnFeO3-δ (Ln=La, Pr and Gd) perovskite cathodes, J. Power Sources. 485 (2021) 229343. doi:https://doi.org/10.1016/j.jpowsour.2020.229343.

[33] L. Zhong, T. Kropp, W. Baaziz, O. Ersen, D. Teschner, R. Schlögl, M. Mavrikakis, S. Zafeiratos, Correlation between Reactivity and Oxidation State of Cobalt Oxide Catalysts for CO Preferential Oxidation, ACS Catal. 9 (2019) 8325–8336. doi:10.1021/acscatal.9b02582.

[34] S. Turczyniak, D. Teschner, A. Machocki, S. Zafeiratos, Effect of the surface state on the catalytic performance of a Co/CeO2 ethanol steam-reforming catalyst, J. Catal. 340 (2016) 321–330. doi:10.1016/j.jcat.2016.05.017.

[35] V. Papaefthimiou, D.K. Niakolas, F. Paloukis, T. Dintzer, S. Zafeiratos, Is Steam an Oxidant or a Reductant for Nickel/Doped-Ceria Cermets?, ChemPhysChem. 18 (2017) 164–170. doi:10.1002/cphc.201600948.

[36] V. Papaefthimiou, M. Shishkin, D.K. Niakolas, M. Athanasiou, Y.T. Law, R. Arrigo, D. Teschner, M. Hävecker, A. Knop-Gericke, R. Schlögl, T. Ziegler, S.G. Neophytides, S. Zafeiratos, On the active surface state of nickel-ceria solid oxide fuel cell anodes during methane electrooxidation, Adv. Energy Mater. 3 (2013) 762–769. doi:10.1002/aenm.201200727.

[37] J.J. Yeh, I. Lindau, Atomic subshell photoionization cross sections and asymmetry parameters: 1 <Z< 103, At. Data Nucl. Data Tables. 32 (1985) 1–155. doi:10.1016/0092-640X(85)90016-6.

[38] M.A. Henderson, C.L. Perkins, M.H. Engelhard, S. Thevuthasan, C.H.F. Peden, Redox

properties of water on the oxidized and reduced surfaces of CeO2(1 1 1), Surf. Sci. 526 (2003) 1–18. doi:10.1016/S0039-6028(02)02657-2.
[39] M. Canavar, Y. Kaplan, Effects of mesh and interconnector design on solid oxide fuel cell performance, Int. J. Hydrogen Energy. 40 (2015) 7829–7834. doi:https://doi.org/10.1016/j.ijhydene.2014.11.101.
[40] A. Schaefer, B. Hagman, J. Höcker, U. Hejral, J.I. Flege, J. Gustafson, Thermal reduction of ceria nanostructures on rhodium(111) and re-oxidation by CO2, Phys. Chem. Chem. Phys. 20 (2018) 19447–19457. doi:10.1039/c8cp01505h.
[41] T. Staudt, Y. Lykhach, N. Tsud, T. Skála, K.C. Prince, V. Matolín, J. Libuda, Ceria reoxidation by CO2: A model study, J. Catal. 275 (2010) 181–185. doi:10.1016/j.jcat.2010.07.032.
[42] D. Chen, M. Barreau, T. Dintzer, F. Bournel, J.-J. Gallet, S. Zafeiratos, Surface oxidation of Ni-cermet electrodes by CO2 and H2O and how to moderate it, J. Energy Chem. under revi (2021).
[43] A. Nenning, M. Holzmann, J. Fleig, A.K. Opitz, Excellent kinetics of single-phase Gd-doped ceria fuel electrodes in solid oxide cells, Mater. Adv. 2 (2021) 5422–5431. doi:10.1039/D1MA00202C.
[44] P.I. Giotakos, S.G. Neophytides, Physical modeling of the electrochemical impedance spectra for the O2 reduction reaction in HTPEM fuel cells' cathodic electrochemical interface, Electrochim. Acta. 292 (2018) 285–291. doi:https://doi.org/10.1016/j.electacta.2018.08.141.
[45] A.A. Kulikovsky, The regimes of catalyst layer operation in a fuel cell, Electrochim. Acta. 55 (2010) 6391–6401. doi:https://doi.org/10.1016/j.electacta.2010.06.053.
[46] T. Hong, Y. Zhang, K. Brinkman, Enhanced Oxygen Electrocatalysis in Heterostructured Ceria Electrolytes for Intermediate-Temperature Solid Oxide Fuel Cells, ACS Omega. 3 (2018) 13559–13566. doi:10.1021/acsomega.8b02127.
[47] W.H. Doh, V. Papaefthimiou, T. Dintzer, V.V. Dupuis, S. Zafeiratos, Synchrotron radiation X-ray photoelectron spectroscopy as a tool to resolve the dimensions of spherical core/shell nanoparticles, J. Phys. Chem. C. 118 (2014) 26621–26628. doi:10.1021/jp508895u.
[48] C. Dueso, M. Ortiz, A. Abad, F. García-Labiano, L.F. De Diego, P. Gayán, J. Adánez, Reduction and oxidation kinetics of nickel-based oxygen-carriers for chemical-looping combustion and chemical-looping reforming, Chem. Eng. J. 188 (2012) 142–154. doi:10.1016/j.cej.2012.01.124.
[49] D. Knapp, T. Ziegler, Methane dissociation on the ceria (111) surface, J. Phys. Chem. C. 112 (2008) 17311–17318. doi:10.1021/jp8039862.
[50] S. Zafeiratos, S. Kennou, The interaction of oxygen with ultrathin Ni deposits on yttria-stabilized ZrO2(1 0 0), Surf. Sci. 482–485 (2001) 266–271. doi:10.1016/S0039-6028(01)00929-3.
[51] I.-K. Oh, L. Zeng, J.-E. Kim, J.-S. Park, K. Kim, H. Lee, S. Seo, M.R. Khan, S. Kim, C.W. Park, J. Lee, B. Shong, Z. Lee, S.F. Bent, H. Kim, J.Y. Park, H.-B.-R. Lee, Surface Energy Change of Atomic-Scale Metal Oxide Thin Films by Phase Transformation, ACS Nano. 14 (2020) 676–687. doi:10.1021/acsnano.9b07430.
[52] T. Montini, M. Melchionna, M. Monai, P. Fornasiero, Fundamentals and Catalytic Applications of CeO2 -Based Materials, Chem. Rev. 116 (2016) 5987–6041. doi:10.1021/acs.chemrev.5b00603.

[53] S. Gunduz, D.J. Deka, U.S. Ozkan, Advances in High-Temperature Electrocatalytic Reduction of CO2 and H2O, Adv. Catal. 62 (2018) 113–165. doi:10.1016/bs.acat.2018.08.003.
[54] J. Wang, S.R. Bishop, L. Sun, Q. Lu, G. Vardar, R. Bliem, N. Tsvetkov, E.J. Crumlin, J.-J.J. Gallet, F. Bournel, I. Waluyo, B. Yildiz, Threshold catalytic onset of carbon formation on CeO2 during CO2 electrolysis: Mechanism and inhibition, J. Mater. Chem. A. 7 (2019) 15233–15243. doi:10.1039/c9ta03265g.
[55] Z.A. Feng, C. Balaji Gopal, X. Ye, Z. Guan, B. Jeong, E. Crumlin, W.C. Chueh, Origin of Overpotential-Dependent Surface Dipole at CeO2-x/Gas Interface during Electrochemical Oxygen Insertion Reactions, Chem. Mater. 28 (2016) 6233–6242. doi:10.1021/acs.chemmater.6b02427.
[56] A. Faes, Q. Jeangros, J.B. Wagner, T.W. Hansen, J. Van Herle, A. Brisse, R. Dunin-Borkowski, A. Hessler-Wyser, In situ Reduction and Oxidation of Nickel from Solid Oxide Fuel Cells in a Transmission Electron Microscope, ECS Trans. 25 (2019) 1985–1992. doi:10.1149/1.3205743.
[57] F.S. Torknik, M. Keyanpour-Rad, A. Maghsoudipour, G.M. Choi, Effect of microstructure refinement on performance of Ni/Ce0.8Gd0.2O1.9 anodes for low temperature solid oxide fuel cell, Ceram. Int. 40 (2014) 1341–1350. doi:https://doi.org/10.1016/j.ceramint.2013.07.015.
[58] E. Lay-Grindler, J. Laurencin, J. Villanova, P. Cloetens, P. Bleuet, A. Mansuy, J. Mougin, G. Delette, Degradation study by 3D reconstruction of a nickel-yttria stabilized zirconia cathode after high temperature steam electrolysis operation, J. Power Sources. 269 (2014) 927–936. doi:10.1016/j.jpowsour.2014.07.066.
[59] M. Chen, J.V.T. Høgh, J.U. Nielsen, J.J. Bentzen, S.D. Ebbesen, P.V. Hendriksen, High Temperature Co-Electrolysis of Steam and CO2 in an SOC Stack: Performance and Durability, Fuel Cells. 13 (2013) 638–645. doi:https://doi.org/10.1002/fuce.201200169.
[60] E. Ioannidou, C. Neofytidis, L. Sygellou, D.K. Niakolas, Au-doped Ni/GDC as an Improved Cathode Electrocatalyst for H2O Electrolysis in SOECs, Appl. Catal. B Environ. 236 (2018) 253–264. doi:10.1016/j.apcatb.2018.05.017.
[61] C. Neofytidis, E. Ioannidou, L. Sygellou, M. Kollia, D.K. Niakolas, Affecting the H2O electrolysis process in SOECs through modification of NiO/GDC; experimental case of Au-Mo-Ni synergy, J. Catal. 373 (2019) 260–275. doi:https://doi.org/10.1016/j.jcat.2019.04.002.
[62] X.K. Gu, E. Nikolla, Fundamental Insights into High-Temperature Water Electrolysis Using Ni-Based Electrocatalysts, J. Phys. Chem. C. 119 (2015) 26980–26988. doi:10.1021/acs.jpcc.5b07814.
[63] D. Sarantaridis, A. Atkinson, Redox Cycling of Ni-Based Solid Oxide Fuel Cell Anodes: A Review, Fuel Cells. 7 (2007) 246–258. doi:https://doi.org/10.1002/fuce.200600028.